

**REVISION 1**

**High-temperature behavior of natural ferrierite:  
In-situ synchrotron X-ray powder diffraction study**

Rossella Arletti<sup>a,b</sup>, Riccardo Fantini<sup>c</sup>, Carlotta Giacobbe<sup>d</sup>, Reto Gieré<sup>e</sup>,  
Giovanna Vezzalini<sup>c</sup>, Ruggero Vigliaturo<sup>c</sup>, and Simona Quartieri<sup>f\*</sup>

<sup>a</sup> *Dipartimento di Scienze della Terra, Università di Torino, via Valperga Caluso 35, 10125 Torino, Italy.*

<sup>b</sup> *Centro Interdipartimentale “Nanostructure Interfaces and Surfaces NIS”,  
Via Pietro Giuria 7, 10125 Torino, Italy*

<sup>c</sup> *Dipartimento di Scienze Chimiche e Geologiche,  
Università di Modena e Reggio Emilia, via Campi 103, 41125 Modena, Italy.*

<sup>d</sup> *ESRF-European Synchrotron Radiation Facility, CS 40220  
38043 Grenoble Cedex 9, Grenoble, France*

<sup>e</sup> *Department of Earth and Environmental Science, and Center of Excellence in Environmental Toxicology,  
University of Pennsylvania, 240 S. 33rd Street, Hayden Hall, Philadelphia, PA 19104-6316, U.S.A.*

<sup>f</sup> *Dipartimento di Scienze Matematiche e Informatiche, Scienze Fisiche e Scienze della Terra,  
Università di Messina, viale F. Stagno d'Alcontres 31, 98166 Messina S. Agata, Italy.*

## ABSTRACT

In this paper we report results of the first study focused on the thermal stability and dehydration dynamics of the natural zeolite mineral ferrierite. A sample from Monastir, Sardinia  $[(\text{Na}_{0.56}\text{K}_{1.19}\text{Mg}_{2.02}\text{Ca}_{0.52}\text{Sr}_{0.14})(\text{Al}_{6.89}\text{Si}_{29.04})\text{O}_{72}\cdot 17.86\text{H}_2\text{O}; a=19.2241(3)\text{\AA}; b=14.1563(2)\text{\AA}; c=7.5106(1)\text{\AA}, V=2043.95(7)\text{\AA}^3]$  was investigated by thermogravimetric analysis and *in-situ* synchrotron X-ray powder diffraction. Thermogravimetric data show that  $\text{H}_2\text{O}$  release begins already in the range 50-100 °C and is complete at ~ 600°C. The results of the structure refinements performed in *Immm* s.g. by Rietveld analysis with data collected up to 670°C show that ferrierite belongs to the group of zeolites that do not undergo phase transitions. Upon heating to 670°C, ferrierite behaves as a non-collapsible structure displaying only a slight contraction of the unit-cell volume ( $\Delta V= -3\%$ ). The unit-cell parameter reductions are anisotropic, more pronounced for *a* than for *b* and *c* ( $\Delta a= -1.6\%$ ;  $\Delta b= -0.76\%$ ;  $\Delta c= -0.70\%$ ). This anisotropic response to a temperature increase is interpreted as due to the presence in the ferrierite framework of five-membered ring chains of  $\text{SiO}_4$  tetrahedra, which impart a higher structural rigidity along *b* and *c*. Upon dehydration we observe: i) the gradual  $\text{H}_2\text{O}$  loss, beginning with the molecules hosted in the 10MR channel, is almost complete at 670°C, in good agreement with the TG data; ii) as a consequence of the decreased  $\text{H}_2\text{O}$  content, Mg and K migrate from their original positions, moving from the center of the 10MR channel towards the walls to coordinate the framework oxygen atoms. The observation of transmission electron microscopy selected area electron diffraction patterns revealed defective crystals with an occasional and moderate structural disorder. Beyond providing information on the thermal stability and behavior of natural ferrierite, the results of this work have significant implications for possible technological applications. These data allow for comparison with the dehydration kinetics/mechanisms of the corresponding synthetic phases, clarifying the role played by framework and extra-framework species on the high-temperature behavior of porous materials with ferrierite topology. Moreover, the information on the thermal behavior of natural ferrierite can be used to predict the energetic performances of analogous synthetic Si-pure counterparts, namely “zeosil-

electrolyte” systems, under non-ambient conditions. Specifically, the very high thermal stability of ferrierite determined in this study, coupled with the baric behavior determined in other investigations, suggests that the “Si-FER–electrolyte” system may be an excellent candidate for use as energy reservoir. Indeed, ferrierite exhibits the so-called “spring behavior”, i.e., upon compression in water or in an electrolyte solution, it converts the mechanical energy into an interfacial energy, and – when pressure is released – it can completely restore the supplied mechanical energy accumulated during the compression step.

**Keywords:** Zeolite, ferrierite, thermal behavior, high-temperature synchrotron X-ray powder diffraction, structure refinement, TEM, TGA.

## INTRODUCTION

The thermal behavior (i.e., stability, phase transformations, rate and temperature of dehydration, rehydration) is one of the most interesting properties of both natural zeolites and microporous synthetic materials. It has been widely studied because all the processes occurring at high temperature deeply influence the sorptive and catalytic properties of these phases. Hence, knowledge of the structural modifications of zeolites induced by temperature is fundamental both to define their stability field as minerals, and to assure their persistence and effectiveness in their numerous technological applications.

Several authors have contributed to developing a classification scheme of the dehydration behavior of zeolite materials (see Alberti and Vezzalini, 1984; Bish and Carry, 2001; Cruciani, 2006, Alberti and Martucci, 2011 for a review), differentiating their response to temperature increase mainly on the basis of this classification: *i)* zeolites that undergo dehydration accompanied by rearrangement of the cations, but without significant changes in the framework structure and unit-cell volume; *ii)* zeolites that undergo significant framework distortion and reduction of unit-cell volume, but do not change their topology up to the collapse or breakdown, and *iii)* zeolites that undergo topological changes in the framework, due to the breaking of T-O-T bridges and the migration of the tetrahedral cations to new tetrahedral sites. In particular, the thermal behavior of this last zeolite group has been studied in detail by many authors and was recently reviewed in Arletti et al. (2013).

Another well-known classification of zeolite heating behavior was proposed by Baur (1992), who divided zeolite frameworks into a) ‘non-collapsible’, where the presence of anti-rotating T–O–T hinges provides them with a distortion self-limiting mechanism; and as b) ‘collapsible’, where the presence of co-rotating hinges enhances the distortion of the framework structure.

Among the numerous studies performed in the past on the thermal behavior of zeolites, no specific information is available on natural ferrierite. This gap deserves to be filled, both for the mineralogical interest

in this species, and in view of the paramount importance of its synthetic counterparts in many technological applications. For example, materials with framework-type FER (Baerlocher et al. 2007) are important in the petrochemical industry, where they have been used as shape-selective catalysts for the production of isobutene, and for the selective catalytic reduction of nitrogen oxides (Li et al. 1993). These reactions take place at elevated temperature, so it is essential to study thoroughly the thermal behavior of these materials (Bull et al. 2003; Dalconi et al. 2003).

Natural ferrierite was first reported by Graham (1918) and its structure was first determined by Vaughan (1966). The sample used for this work comes from Monastir, Sardinia (Orlandi and Sabelli, 1983), and its structure was refined by Alberti and Sabelli (1987). Its thermal behavior and stability were investigated here by both thermogravimetric (TG) analysis and *in-situ* high-temperature synchrotron X-ray powder diffraction (XRPD).

Specifically, this work is aimed at:

- i) determining the thermal stability of natural ferrierite;
- ii) continuous monitoring of the thermally-induced H<sub>2</sub>O loss and extra-framework cation migration by means of time-resolved synchrotron XRPD;
- iii) interpreting, from a structural point of view, the thermally-induced modifications of ferrierite unit cell and framework structure;
- iv) evaluating the structural disorder, due to shear faults, present in ferrierite framework, by means of selected area electron diffraction (SAED).

Moreover, and importantly, the results of this work – beyond providing information on the thermal stability and heating behavior of ferrierite mineral – will have significant implications for technological applications. In fact, by comparing our data with the dehydration kinetics and mechanisms of the corresponding synthetic phases (Dalconi et al. 2000; 2003), we will contribute to identifying the role played by framework and extra-framework components on the high-temperature behavior of porous materials with FER topology.

## FERRIERITE STRUCTURE

Ferrierite used for this work comes from Monastir (Sardinia, Italy) (Figure 1). Its chemical composition is  $(\text{Na}_{0.56}\text{K}_{1.19}\text{Mg}_{2.02}\text{Ca}_{0.52}\text{Sr}_{0.14})(\text{Al}_{6.89}\text{Si}_{29.04})\text{O}_{72}\cdot 17.86 \text{ H}_2\text{O}$  (Alberti and Sabelli, 1987). Unit-cell parameters determined in the present study are  $a=19.2241(3) \text{ \AA}$ ;  $b=14.1563(2) \text{ \AA}$ ;  $c=7.5106(1) \text{ \AA}$ ,  $V=2043.95(7) \text{ \AA}^3$ .

The ferrierite framework can be described by chains of rings consisting of five  $\text{SiO}_4$  tetrahedra (known as 5MR building units), which form layers on the  $ab$  plane (Figure 2a). These layers are connected to form channels of ten-membered rings (10MR) running parallel to  $[001]$ , which are intersected by channels of eight-membered rings (8MR) running parallel to  $[010]$  (Figure 2b). Six-membered rings (6MR) connect the 10MRs channels along  $[010]$ . The framework contains cavities known as the “ferrierite cage”, formed by the intersection of the 8MR and the 6MR channels (parallel to the  $c$  axis).

The topological symmetry of ferrierite is orthorhombic  $Immm$  (Vaughan 1966). However, deviations from this symmetry are well known and depend on both extra-framework and framework content. Although the  $Immm$  s. g. was successfully used by Alberti and Sabelli (1987) in their structure refinement of the natural Mg-rich ferrierite from Monastir (abbreviated below as MON-FER), the real symmetry was consistent with the subgroup  $Pnmm$ . In particular, the structure refinement in the centrosymmetric s.g.  $Immm$  constrains the framework oxygen O5 to a symmetry center, so that the T4-O5-T4 angle assumes a value of  $180^\circ$ , which is not energetically favored. As reported by Alberti and Sabelli (1987) for MON-FER, Mg is coordinated by six  $\text{H}_2\text{O}$  molecules, in an almost regular octahedral configuration, at the center of the “ferrierite cage”. Magnesium lies on a site of  $mmm$  symmetry, two of the six  $\text{H}_2\text{O}$  molecules are along the  $z$  axis in a  $mm$  site symmetry, and the other four are in the  $xy$  plane. This  $\text{Mg}(\text{H}_2\text{O})_6$  octahedron, however, has two possible configurations, which occur 50% of the time and differ by a rotation of about  $45^\circ$  around the  $z$  axis. The orientation of each of these two configurations disobeys  $Immm$  symmetry, and the true symmetry lowers to the subgroup  $Pnmm$ . In this s.g., O5 is no longer constrained to the inversion center and the straight T4-O5-

T4 angle is thus only apparent, derived from the equal statistical occupation of two O5 sites, moved from the inversion center.

Regarding other structural refinements of natural ferrierites reported in the literature, the Mg-poor, Na-K-rich sample from Altoona, Washington, studied by Gramlich-Meier et al. (1985), crystallizes in the monoclinic  $P2_1/n$  symmetry, whereas Yokomori et al. (2001) described a natural ferrierite from Kamloops Lake in s.g.  $I222$ . Ferrierite from Silver Mountain, California (Gramlich-Meier, 1984) was refined in  $Immm$ .

The monoclinic s.g.  $P2_1/n$  found by Gramlich-Meier et al. (1985) for the Altoona ferrierite was also found by Cruciani et al. (1999) for the as-synthesized K,Na-rich low-silica ferrierite. This lowering of symmetry was explained by the authors as a consequence of the distortion of the 8MR caused by K and Na cations in a site near, but significantly displaced from, the center of the 8-ring, in order to allow for a better coordination environment.

Morris et al. (1994) described the all-silica synthetic ferrierite in the orthorhombic  $Pmnn$  s.g., whereas Bull et al. (2003) described a temperature-dependent second-order displacive phase transition from a low-symmetry ( $Pnmm$ ) to a high-symmetry ( $Immm$ ) structure, associated with a change from positive to negative thermal expansion behavior. In other structure refinements of both hydrated and dehydrated ferrierites, the topological symmetry  $Immm$  was assumed (Pickering et al. 1989; Attfield et al. 1997; Martucci et al. 1999; Dalconi et al. 2000; Darton and Morris 2006), even when there was evidence that the real symmetry was lower.

Beyond the effects of the framework deformations and of the extra-framework cation coordination polyhedra, structural defects, observed frequently in ferrierite, have also been invoked as a factor that strongly influences the properties and the real space group of this zeolite. Gramlich-Meier et al. (1984), Sanders (1985) and Smith (1986), on the basis of electron diffraction data, proposed a number of defect structures the ferrierite framework might support, possibly lowering the symmetry: these involve mainly  $\sigma$  transformations of the type suggested by Shoemaker et al. (1973), in which sheets of tetrahedra are either subtracted (contraction fault) or added (expansion fault). Rice et al. (1994) studied the planar defects

suggested by electron diffraction patterns of ferrierite from Lovelock (Nevada). By means of modeling and diffraction simulations, these authors proposed a number of possible candidate fault structures, and – on the basis of the comparison among the experimental and the simulated powder patterns – they found that in this ferrierite the most common faults involve a  $c/2$  shear on the (040) plane, with a frequency up to 30%, and a  $c/2$  shear on the (400) plane, with a frequency of only about 5%. The effects of the framework disorder in ferrierite from Monastir will be further discussed below based on SAED patterns.

## EXPERIMENTAL METHODS

### Thermogravimetric (TG) analysis

TG analysis of MON-FER was carried out using a Seiko SSC/5200 thermal analyzer. About 5 mg of sample were loaded into a Pt crucible and heated in air from room temperature to 950 °C, with a heating rate of 5 °C/min. TG and differential thermogravimetric (DTG) curves are shown in Figure 3.

### Selected Area Electron Diffraction (SAED) study

The MON-FER powder sample was dispersed in 2-propanol and gently hand-ground in an agate mortar to obtain a homogeneous suspension in which individual particles were not visible with the naked eye. A droplet of the suspension was transferred onto a 300-mesh holey-carbon copper TEM grid. The SAED study was performed using a JEOL 2010F TEM at an operating voltage of 200 kV. The TEM is equipped with a double-tilt sample holder. After inserting the holder into the TEM, the sample was left within the column for 30 minutes before exposing it to the electron beam to allow it to desiccate and to reduce subsequent electron beam damage (Rice et al. 1994). Several stability tests were performed to assess the specimen's resistance to the electron beam using a spot size = 2,  $\alpha = 3$ , and SAED diaphragm of 50  $\mu\text{m}$  to keep the electron density of the beam low. After these tests we decided to discard all SAED patterns that we were unable to orient and record in less than 30 seconds from the first active exposure to the electron beam.



## Synchrotron X-ray powder diffraction (XRPD) experiments

The temperature-resolved synchrotron XRPD patterns were collected at the ID22 beamline of the ESRF (Grenoble) with a fixed wavelength of 0.3999 Å (calibrated with Si NIST standard reference material). The sample was ground with an agate mortar to a crystallite dimension of 9-10 μ and then loaded and packed into a 0.3 mm silica glass capillary. The capillary was mounted on a standard goniometric head and kept spinning during pattern collection. The sample was heated in-situ using a hot-air blower from room  $T$  (30°C) to 670 °C with a heating rate of 5 °C/min. Temperature was calibrated with the thermal expansion of a Pt reference standard material. Diffraction patterns were recorded with a high-resolution multi-analyzer stage composed of nine analyzer crystals in the  $2\theta$  range 0–28°. Between 50 and 650°C the patterns were collected every 50 °C. Selected powder patterns are reported in Figure 4S (Appendix<sup>1</sup>).

The GSAS package (Larson and Von Dreele, 2000) with the EXPGUI interface (Toby, 2001) was used for Rietveld refinement. The adopted starting coordinates and site symbols are from Alberti and Sabelli (1987). With the real ferrierite space group still under debate, both  $Pmnn$  and  $Immm$  s.g. were adopted for the structure refinements over the entire  $T$  range investigated. However, the  $RF^{**2}$  of the structure refinements performed in the two s.g. were comparable (9.09 and 9.68 for  $Pmnn$  and  $Immm$  s.g., respectively) and no strong indication of a symmetry lowering to  $Pmnn$  s.g. was found. Hence only the results obtained in the topological  $Immm$  s.g. are presented and discussed in the following.

## Structure refinements

The Bragg-peak profiles were modeled by a pseudo-Voigt function (Thomson et al. 1987) with a peak intensity cut-off set to 0.001 of the peak maximum. Due to the presence of planar defects, evidenced by SAED patterns (see below), the anisotropic contribution of the Lorentzian broadening along [200] (“stec” and “ptec” in the GSAS code; Larson and Von Dreele 2000) were refined. The background curve was fit with an 18-term Chebyshev polynomial. The overall scale factor, the  $2\theta$ -zero shift, and the unit-cell parameters

were refined for each histogram over the entire temperature range. Neutral atom scattering curves were used for all species. Soft constraints were imposed on the tetrahedral bond lengths T-O (1.63 Å), with a tolerance value of 0.03. Isotropic thermal displacement parameters were constrained in order to have the same value for the same atomic species. At high temperature, the Uiso values of the original Mg and K sites became progressively unreasonable - as a consequence of cation migration towards new site positions (Mg2 and K2) and of the increasing disorder - and hence were fixed to the values refined for Mg2 and K2, respectively. The occupancy factors of the Mg and Mg2 sites were constrained to a sum of 100%. The refined structural parameters for each histogram were as follows: fractional coordinates and isotropic displacement factors for all atoms, and occupancy factor only for the extra-framework species. After the Mg-site splitting, the sum of Mg and Mg2 occupancy factors was constrained to the initial Mg-site value.

Table 1 reports the unit-cell parameters refined up to 670°C, and Figure 5 shows the normalized unit-cell parameters as a function of *T*. The final observed and calculated powder patterns at 30, 200, 300, 450 and 670 °C are shown in Figure 6S (Appendix<sup>1</sup>). For the same selected temperatures, the refinement details are summarized in Table 2, and Tables 1S and 2S (Appendix<sup>1</sup>) report the atomic coordinates and the bond distances of tetrahedral and extra-framework species, respectively.

## RESULTS AND DISCUSSION

### Thermogravimetric analysis

The TG analysis of MON-FER (Figure 3) shows that H<sub>2</sub>O release begins from the very early heating stages and is complete at about 600°C, with a DTG maximum at 159°C (the maximum rate of H<sub>2</sub>O loss). The cumulative weight loss is 14%, corresponding to 20.5 H<sub>2</sub>O molecules p.f.u., which compares to 17.86 and 23.12 molecules found by Alberti and Sabelli (1987) for ferrierite from the same locality from chemical analysis and structural refinement, respectively.

## Selected Area Electron Diffraction study

The TEM investigation reveals a moderate structural disorder in the studied sample. Streaks in SAED patterns, when present, have several orientations relative to the detected crystal planes (Figure 7). Striking is most pronounced along the [200] crystallographic direction (Figure 7b).

## Structure refinements

As described in the Experimental section, two series of structure refinements were performed in both *Pmnn* and *Immm* s.g. with the aim of evaluating the symmetry of MON-FER. The results obtained at all investigated temperatures are virtually identical and hence, only the structural data obtained in the high-symmetry *Immm* s.g. are reported in Tables and Figures. The initial mismatch in the intensities (and broadening) of the (200) and (040) reflections, observed for the refinement at 30°C in both the s.g., was solved after accurate profile refinement. The anisotropic broadening coefficient points, in agreement with the SAED results, to the presence of some disorder along the [200] crystallographic direction.

## Unit-cell variations upon heating

The variations of the MON-FER unit-cell parameters over the investigated *T* range (Table 1, Figure 5) are anisotropic, more pronounced for *a* than for the *b* and *c* axes ( $\Delta a = -1.6\%$ ;  $\Delta b = -0.76\%$ ;  $\Delta c = -0.70\%$ ). Moreover, although *b* and *c* decrease in a progressive way over the entire *T* range, most of the change in *a* occurs below 350-400°C. From 400 to 670 °C, the *a* unit-cell parameter undergoes a very slight increase (of about 0.15%). These behaviors will be interpreted below on the basis of the structure refinement data.

These heating-induced modifications can be compared with those of two exchanged ferrierite samples, which were studied previously at high *T*: Co-exchanged ferrierite ( $\text{Na}_{0.2}\text{Co}_{1.8}\text{Al}_{3.8}\text{Si}_{32.2}\text{O}_{72}\cdot 18\text{H}_2\text{O}$ ; Co-FER), progressively dehydrated from room *T* to 810°C (Dalconi et al. 2003), and Ni-exchanged ferrierite ( $\text{Na}_{0.2}\text{Ni}_{1.9}\text{Al}_{3.8}\text{Si}_{32.2}\text{O}_{72}\cdot 18\text{H}_2\text{O}$ ; Ni-FER), directly heated at 600°C (Dalconi et al. 2000). Both of these exchanged phases show anisotropic behavior in the unit-cell parameter contractions similar to that found for

MON-FER: upon heating, the strongest shortening was observed along the *a* axis (-1.26% and -1.08% in Co-FER and Ni-FER, respectively), whereas the smallest shortening (-0.35% and virtually 0% in Co-FER and Ni-FER, respectively) is registered along the *c* axis. This behavior is not surprising, considering that *c* is parallel to the direction of the five-ring chains forming the FER framework (Figure 2) and that the *bc* plane is the densest part of the framework.

Overall, dehydration of MON-FER is accompanied by a total volume decrease of 3%, comparable to that observed for Co-FER (2.35%, Dalconi et al. 2003) and slightly greater than that of Ni-FER (1.4%, Dalconi et al. 2000). These small contractions of the unit-cell volume confirm that ferrierite is characterized by a non-collapsible behavior upon heating (Baur, 1992).

### **Structure of MON-FER at room conditions**

From the structure refinement of MON-FER at room conditions (Figure 8a and Appendix<sup>1</sup> Table 1S), six H<sub>2</sub>O sites, corresponding to 23.29 H<sub>2</sub>O molecules p.f.u., and two extra-framework cation sites were located. The cation positions were refined with Mg and K scattering curves resulting in 1.98 Mg and 1.76 K p.f.u. The total cation content (2 Mg and 1.64 K p.f.u.) and the amount of H<sub>2</sub>O (23.12 molecules p.f.u.) are in very good agreement with those found by Alberti and Sabelli (1987) in their structural refinement of ferrierite from the same locality (i.e., 2.02 Mg, 1.19 K, 0.56 Na, 0.52 Ca, 0.14 Sr and 17.86 H<sub>2</sub>O molecules p.f.u.).

The Mg site is bonded to two W1, two W2 and two W3 H<sub>2</sub>O molecules, in a slightly distorted octahedron (Appendix<sup>1</sup> Table 2S), characterized by a Mg-W3 bond that is slightly longer (2.29 Å) than the other two coordination distances. As in Alberti and Sabelli (1987), the Mg coordination polyhedron has two possible orientations, that occur 50% of the time and differ by a rotation of ~ 45° around the *z* axis. The K site is bonded to four O8 framework oxygen atoms and to four H<sub>2</sub>O molecules, distributed over the W5 and W6 sites.

## H<sub>2</sub>O release and cation migrations induced by heating

The results of the structure refinements performed at elevated  $T$  (Appendix<sup>1</sup> Tables 1S, 2S; Figure 8 b,c,d,e; Figure 9 b,c,d,e and Figure 10) confirm the results of the TG measurements, namely that H<sub>2</sub>O loss begins already in the range 50-100 °C, by first involving the W1, W4, W5 and W6 sites. Subsequently, in the range 100-150°C, the W1, W4 and W6 occupancies continue to decrease. At 150°C, the Mg-W3 bond becomes too long (2.54 Å), and Mg remains 4-fold coordinated only to W1 and W2. In fact, the 6-fold coordination is hindered by the W2-W2 distance (about 1.8 Å), which is too short and thus requires that only one of the two positions can be occupied by H<sub>2</sub>O simultaneously. This situation triggers the gradual migration, observed at 200°C, of Mg<sup>2+</sup> towards the new site labeled Mg2 (Figures 8b, 9b, 10), located at the center of the 6MR window of the FER cage (0,0,0 site), where it is coordinated to four O3 oxygen atoms. The new site Mg2 is similar to that found by Dalconi et al. (2000; 2003) for Ni and Co in Ni-FER and Co-FER, respectively. Specifically, in the case of Co-FER, beginning at about 100 °C, a fraction of the cations in the Co1 site moves toward to a new site labelled Co1a at the center of the six-ring of the cage (but out of the plane of the oxygens by about 0.5 Å). A similar site, labeled Ni1a, was found in the structure of Ni-exchanged ferrierite dehydrated at 600°C.

At 200°C, in addition to Mg, the K site also splits into a new position, labeled K2 (see Figures 8b,9b), coordinated to two O6, four O7, one W2 and one W4. The K site remains bonded to four O8 and to four W5 and W6 sites (occupied at 15 and 27%, respectively). At this  $T$ , all the H<sub>2</sub>O sites of MON-FER are involved in the dehydration process and only 15.5 H<sub>2</sub>O molecules p.f.u. remain (Figure 10).

In the 200-300°C range, the Mg/Mg2 ratio decreases due to a further migration of Mg towards the new Mg2 site. Moreover, almost all the H<sub>2</sub>O sites undergo a significant decrease in occupancy (Figure 8 and Appendix<sup>1</sup> Table 1S). Specifically, at 250°C, the W2, W5 and W6 occupancies are significantly reduced to 0.19, 0.29 and 0.19, respectively. In addition, at 300°C, W5 moves from its position towards the symmetry plane at  $z=0.50$ . Interestingly, at this  $T$ , the reciprocal W2-W2 distance (very short at lower  $T$ ) increases to about 3.0 Å (Appendix<sup>1</sup> Table 2S), allowing for the residual Mg site to regain its original octahedral

coordination, now bonding to two W1 and four W2 sites (Figures 8c, 9c).

Between 300 and 350°C, due to the rather unsatisfactory coordination spheres of the original Mg and K sites, both Mg/Mg<sub>2</sub> and K/K<sub>2</sub> ratios decrease further. At 350°C the residual H<sub>2</sub>O content corresponds to 7.16 molecules p.f.u. (Figure 10).

At 400°C, the W6 H<sub>2</sub>O molecule is completely lost, and W4 moves from its previous position to improve the coordination polyhedron of the K site. Specifically, the new W4 position is intermediate between that of the original W4 and W6 sites. Starting from this temperature, the K site loses its coordination with the framework oxygen atom O8, thus inducing the above-mentioned slight *a* axis expansion. At this *T*, Mg<sub>2</sub> also changes its position, in this case moving outside the symmetry plane at *z*=0.0. At this *T*, the Mg<sub>2</sub> position corresponds exactly to that of the Co1a site of Dalconi et al. (2003). Due to the site shift, Mg<sub>2</sub> remains coordinated to four O3 oxygen atoms, but to only one W1 H<sub>2</sub>O molecule, reducing its coordination from 6 to 5.

The six-fold coordination of Mg<sub>2</sub> is regained at 450°C (Figures 8d, 9d), as a result of the splitting of the O1 oxygen site over a new position O1bis (Appendix<sup>1</sup> Tables 1S, 2S), shifted toward the center of the FER cage. Under these conditions, the Mg<sub>2</sub> site is 6-fold coordinated to four O3 and two O1bis oxygen atoms. Dalconi et al. (2003) observed a very similar behavior during the dehydration of Co-FER: at 100°C the increase in occupancy of the new Co1a site is accompanied by a shift of O1 oxygen toward the center of the six-ring window, and consequently toward the Co1a site.

At 550°C, the K site is minimally occupied, accounting for only 0.3 atoms p.f.u. (Figure 10). To maintain its bonding with the W4 H<sub>2</sub>O molecule, which is migrating upon heating, the K site moves on the plane at *x*=0.50. At this *T*, we observe the complete loss of the W5 molecule and a total remaining H<sub>2</sub>O amount of 5.2 molecules (Figure 10).

Between 550 and 670°C, we observe the progressive decrease of the Mg and K populations in favor of Mg<sub>2</sub> and K<sub>2</sub>, respectively. Again, this is driven by the very poor coordination of the original Mg and K sites, dictated by the H<sub>2</sub>O loss (Figures 8e, 9e). However, these positions continue to host some cations up to

the highest investigated  $T$ . Specifically, at 670°C, 0.13 and 0.36 cations p.f.u. remain in the K and Mg sites, respectively (Figure 10).

At 670°C, 4.3 H<sub>2</sub>O molecules p.f.u. – spread over W2, W3 and W4 sites – were found, indicating only partial dehydration even at the highest investigated temperature (Figure 10). The incomplete dehydration, with respect to the TG data at this  $T$ , can be ascribed to the different experimental conditions of the thermogravimetric and diffractometric measurements (i.e., completely open crucible vs. a capillary open only at one side).

### **Framework structural distortions induced by heating**

As discussed above, the small unit-cell contractions observed in the investigated  $T$  range – mainly due to the decrease in the  $a$  unit-cell parameter below 350-400°C – indicate that ferrierite is characterized by a non-collapsible behavior upon heating (Baur, 1992). This thermal stability is confirmed by the relatively small modifications of the MON-FER framework, which can be attributed mainly to deformations, along the  $a$  axis, of the 6-membered rings and of both 8MR and 10MR channel apertures. Specifically, as reported in Table 3, high  $T$  induces shortening of the O8-O8 and O7-O7 distances, the dimensions along the  $a$  axis of the 10MR and of the 8MR channels, respectively (Figures 8 and 9), and flattening of the 6MR channel along O3-O3 (Figure 8). It is interesting to note that the decrease in these aperture diameters occurs mainly from 30 to 300°C, i.e. in the  $T$  range corresponding to the steepest decrease of the  $a$  unit-cell parameter and unit-cell volume (Figure 5), and to the primary loss of H<sub>2</sub>O (Figures 3 and 10).

The most evident topological modification induced by heating in the MON-FER framework occurs at about 450°C, when the O1 oxygen splits over a new position O1bis (occupied at about 23%), shifted toward the center of the FER cage. As previously discussed, this split results in a uniform coordination of the magnesium cations hosted by the Mg2 site.

## CONCLUDING REMARKS AND IMPLICATIONS

These results of the first study focused on the high-temperature behavior of the natural ferrierite show that it belongs to the group of zeolites that do not undergo phase transitions but only moderate framework deformations. Upon heating to 670°C, it behaves largely as a non-collapsible structure, displaying only a 3% decrease in unit-cell volume, in spite of the loss of almost 24 H<sub>2</sub>O molecules p.f.u. up to 600°C.

These data on MON-FER expand our knowledge of the deformations induced by heating porous minerals. Indeed, due to the lack of information on the dehydration behavior of the natural phase with FER topology, Cruciani (2006) - in his review on the thermal behavior of zeolites - used the data available in the literature for the synthetic Co-FER (Dalconi et al. 2003). However, it is well known that the dehydration kinetics/mechanisms of zeolites are strongly influenced by numerous factors, among which are framework and extra-framework composition. Our results can be integrated into the general models proposed by several authors (see e.g., Breck, 1974; Alberti and Vezzalini, 1984; Baur, 1992; Cruciani, 2006) describing the response of porous minerals to heating, contributing to our understanding of the role played by framework and extra-framework species on zeolite high-temperature stability and to a more complete rationalization of the observed deformation mechanisms.

Further implications of this work concern applications. Recently, our group has developed a research project aimed at the structural study of the energetic performance of hydrophobic silica-zeolites (“zeosils”). Within the framework of this research, we induced the high-pressure intrusion of a MgCl<sub>2</sub> electrolytic aqueous solution into a Si-pure ferrierite (Si-FER) (Arletti et al. 2016). During this intrusion, the mechanical energy is converted into an interfacial energy, and – when pressure is released – the “Si-FER–electrolyte” system can completely restore the supplied mechanical energy accumulated during the compression step, displaying a so-called spring behavior. Interestingly, Arletti et al. (2016) showed that both Mg and Cl penetrate ferrierite channels and that Mg occupies exactly the same position found for this cation in natural ferrierite from Monastir, confirming the preference of Mg for this crystallographic site and demonstrating the



analogies existing between the natural and the synthetic phases. As many technological applications of the “zeosil-electrolyte” systems could involve high-temperature conditions, the results of the present study on the thermal behavior of natural ferrierite can be exploited to predict the energetic performances of the synthetic counterparts as well. In fact, it is reasonable to expect that the cations and the H<sub>2</sub>O molecules moving from the electrolytic solution into the zeolite cavities during the intrusion cycles, occupy crystallographic sites analogous to those present in the natural sample. The very high thermal stability of ferrierite determined here suggests that the “Si-FER–electrolyte” system may be an excellent candidate for an energy reservoir with spring behavior.

### **ACKNOWLEDGEMENTS**

The European Synchrotron Radiation Facility is acknowledged for allocating beam time at the beamline ID22. This work was supported by the Italian MIUR (PRIN2015 Prot. 2015HK93L7). Simona Bigi is acknowledged for the TG analysis, Enrico Bonacina for the macro-photograph of ferrierite sample, and Alessandro Gualtieri for useful discussions. The TEM study was supported in part by grants P30-ES013508 and P42ES023720 awarded by the National Institute of Environmental Health Sciences (NIEHS) The findings are not the official opinions of NIEHS or NIH. David Bish, an anonymous referee, and the guest Editor Diego Gatta are warmly thanked for their comments and suggestions, which greatly improved the quality of the paper.

### **REFERENCES CITED**

Alberti, A., and Martucci, A. (2011) Reconstructive phase transitions in microporous materials: Rules and factors affecting them. *Microporous and Mesoporous Materials*, 141, 192–198.

- Alberti A., and Sabelli, C. (1987) Statistical and true symmetry of ferrierite: possible absence of straight T-O-T bridging bonds. *Zeitschrift für Kristallographie*, 178, 249-256.
- Alberti, A. and Vezzalini, G. (1984) Topological changes in dehydrated zeolites: breaking of T-O-T oxygen bridges. In D. Olson and A. Bisio, Eds., *Proceedings of the 6th International Zeolite Conference*, Reno, 834–841, Butterworths, Guildford, U.K.
- Arletti, R., Vezzalini, G., Quartieri, S., Cámara, F., and Alvaro, M. (2013) A new framework topology in the dehydrated form of zeolite levyne. *American Mineralogist*, 98, 2016-2074.
- Arletti, R., Ronchi, L., Quartieri, S., Vezzalini, G., Ryzhikov, A., Nouali, H., Daou, T. J. , Patarin, J. (2016) Intrusion-Extrusion Experiments of MgCl<sub>2</sub> Aqueous Solution in Pure Silica Ferrierite: Evidence of the Nature of Intruded Liquid by in situ High Pressure Synchrotron X-ray Powder Diffraction. *Microporous and Mesoporous Materials*, 235, 253-260.
- Atfield, M. P., Weigel, S. J., and Cheetham, A. K. (1997) On the nature of nonframework cations in a zeolitic deNO<sub>x</sub> catalyst. *Journal of Catalysis*, 172, 274-280.
- Baerlocher, Ch., McCusker, L.B., and Olson, D.H. (2007) *Atlas of Zeolite Framework Types*, sixth ed., Elsevier, Amsterdam.
- Baur, W.H. (1992) Self-limiting distortion by antirotating hinges of flexible but noncollapsible frameworks, *Journal of Solid State Chemistry*, 97, 243–247.
- Bish, D.L., and Carey, J.W. (2001) Thermal behavior of natural zeolites. In D.L. Bish and D.W. Ming, Eds., *Natural Zeolites: Occurrence, Properties, Applications*, vol. 45, p. 403–452. *Reviews in Mineralogy and Geochemistry*, Mineralogical Society of America, Chantilly, Virginia.
- Bull, I., Lightfoot, Ph., Villaescusa, L.A., Bull, L. M., Gover, R. K. B., Evans, J.S. O., and Morris, R. E. (2003) An X-ray diffraction and MAS NMR study of the thermal expansion properties of calcined siliceous ferrierite. *Journal of the American Chemical Society*, 125, 4342-4349.
- Breck, D.W. (1974) *Zeolite Molecular Sieves*, Wiley, New York.
- Cruciani, G. (2006) Zeolites upon heating: factors governing their thermal stability and structural changes.

Journal of Physics and Chemistry of Solids, 67, 1973–1994.

- Cruciani, G., Alberti, A., Martucci, A., Knudsen, K. D., Ciambelli, P., and Rapacciuolo, M. T. (1999) Crystal structure of zeolite ferrierite in as-synthesized, NH<sub>4</sub>- and H-forms. In Proceeding of the 12th International Zeolite Conference, 1998; Treacy, M. M. J., Markus, B. K., Bisher, M. E., Higgins, J. B., Eds.; Materials Research Society: Warrendale, PA; 2361 -2369.
- Dalconi, M. C., Alberti, A., and Cruciani, G. (2003) Cation migration and structural modification of Co-exchanged ferrierite upon heating: a time-resolved X-ray powder diffraction study. Journal of Physical Chemistry B, 107, 12973-12980.
- Dalconi, M. C., Cruciani, G., Alberti, A., Ciambelli, P., and Rapacciuolo, M. T. (2000) Ni<sup>2+</sup> ion sites in hydrated and dehydrated forms of Ni-exchanged zeolite ferrierite. Microporous and Mesoporous Materials, 39, 423-430.
- Darton, R.J. and Morris, R.E. (2006) High resolution <sup>29</sup>Si MAS NMR study of the thermal behavior of the aluminosilicate zeolite ferrierite. Solid State Sciences, 8, 342-345.
- Granlich-Meier, R., Meier, W.M., and Smith, B.K. (1984) On faults in the framework structure of the zeolite ferrierite. Zeitschrift für Kristallographie, 169, 201-210.
- Gramlich-Meier, R., Gramlich, V., and Meier, W. M. (1985) The crystal structure of the monoclinic variety of ferrierite. American Mineralogist, 70, 619-623.
- Graham, R.P.D. (1918) On ferrierite, a new mineral from British Columbia; with notes on some other Canadian minerals. Transactions of the Royal Society of Canada, 3, 12, 185-201.
- Larson, A.C., and Von Dreele, R.B. (2000) General Structure Analysis System (GSAS). Los Alamos National Laboratory, New Mexico, Report LAUR 86-748.
- Li, Y., and Armor, J. N. (1993) Metal exchanged ferrierites as catalysts for the selective reduction of NO<sub>x</sub> with methane. Applied Catalysis, B: Environmental, 3, L1-L11.
- Martucci, A., Alberti, A., Cruciani, G., Radaelli, P., Ciambelli, P., and Rapacciuolo, M. T. (1999) Location of Brønsted sites in D-ferrierite by neutron powder diffraction. Microporous and Mesoporous

Materials, 30, 95-101.

- Morris, R. E., Weigel, S. J., Henson, N. J., Bull, L. M., Janicke, M. T., Chmelka, B. F., and Cheetham, A. K. (1994) A synchrotron X-ray diffraction, neutron diffraction,  $^{29}\text{Si}$  MAS-NMR, and computational study of the siliceous form of zeolite ferrierite. *Journal of the American Chemical Society* 116, 11849-11855.
- Orlandi, P., and Sabelli, C. (1983) Ferrierite from Monastir, Sardinia, Italy. *Neues Jahrbuch für Mineralogie Monatshefte*, 11, 498-504.
- Pickering, I. J., Maddox, P. J., Thomas, J. M., and Cheetham, A. K. (1989) A neutron powder diffraction analysis of potassium-exchanged ferrierite. *Journal of Catalysis*, 119, 261-265.
- Rice, S.B., Treacy, M.M.J. and Newsam, J.M. (1994) Shear faults in Lovelock ferrierite: An X-ray and electron diffraction analysis. *Zeolites*, 14, 335-343
- Sanders, J.V. (1985) Crystallographic faulting in the mordenite group zeolites. *Zeolites* 1985, 5, 81-90.
- Shoemaker, D.P., Robson, H.E. and Broussard, L. (1973) The 'sigma transformation' interrelating certain known and hypothetical structures. in *Proceeding of the Third International Conference on Molecular Sieves*, 1973, Zurich, pp. 138-143
- Smith, B.K. (1986) Variations in the framework structure of the zeolite ferrierite. *American Mineralogist*, 71, 989-998.
- Thomson, P., Cox, D.E., and Hastings, J.B. (1987) Rietveld refinement of Debye-Scherrer synchrotron X-ray data from  $\text{Al}_2\text{O}_3$ . *Journal of Applied Crystallography*, 20, 79-83.
- Toby, B.H. (2001) EXPGUI, a graphical user interface for GSAS. *Journal of Applied Crystallography*, 34, 210-213.
- Vaughan, P.A. (1966) The crystal structure of the zeolite ferrierite. *Acta Crystallographica*, 21, 983-990.
- Yokomori, Y., Wachsmuth, J., and Nishi, K. (2001) Structure and Brønsted acid sites of ferrierite. *Microporous and Mesoporous Materials*, 50, 137-143.

**Endnote:**

<sup>1</sup>Supplemental Material.

## LIST OF FIGURE CAPTIONS

**Figure 1** – Ferrierite from Monastir (Sardinia). Each aggregate of crystals has a diameter of ~10 mm.

**Figure 2** - Ferrierite framework: **(a)** projection along *c* axis; **(b)** projection along *b* axis.

**Figure 3** - TG (continuous line) and DTG (dashed line) curves of ferrierite

**Figure 4S** – Selected XRPD patterns of ferrierite at increasing temperatures.

**Figure 5** – Normalized unit-cell parameters of ferrierite vs. temperature.

**Figure 6S** – Observed (crossed line) and calculated (continuous line) diffraction patterns and final difference curve from Rietveld refinements of ferrierite at 30 **(a)**, 200 **(b)**, 300 **(c)**, 450 **(d)**, and 670° C **(e)**.

**Figure 7** - SAED images showing streaking running parallel to **(a)** [310] and **(b)** [200]. Image in **(c)** shows the absence of streaks along [020] and [110]. Comparison of Fig. 7a and 7b shows that the streaking can be of different intensity. The [200] streaking is the most common and with the most intense contrast.

**Figure 8** – Projection along *c* axis of ferrierite structure at 30 **(a)**, 200 **(b)**, 300 **(c)**, 450 **(d)**, and 670° C **(e)**.

**Figure 9** – Projection along *b* axis of ferrierite structure at 30 **(a)**, 200 **(b)**, 300 **(c)**, 450 **(d)**, and 670° C **(e)**.

**Figure 10** – **(a)** Total H<sub>2</sub>O content per unit cell, and **(b)** cation site populations vs. temperature.

## TABLES

**Table 1** – Crystallographic data and experimental and refinement parameters for ferrierite at a) 30, b) 200, c) 300, d) 450 and e) 670 °C.

**Table 2** – Unit-cell parameters of ferrierite as a function of temperature.

**Table 3** – Dimensions along the *a* axis of 10MR, 8MR and 6MR at 30, 200, 300, 450 and 670 °C.

**Table 1S** - Atomic coordinates, occupancy factors and thermal parameters for ferrierite structures at 30, 200, 300, 450 and 670 °C.

**Table 2S** – Selected framework and extra-framework bond distance (less than 3.3 Å) at 30, 200, 300, 450, 670 °C. Some non-bonding distances, useful to follow the evolution of the dehydration mechanisms, are reported in italics and are not shown in the Figures.

**Table 1** – Crystallographic data and experimental and refinement parameters for ferrierite at 30, 200, 300, 450 and 670 °C.

T (°C)	30°C	200°C	300°C	450°C	670°C
<b>Space group</b>	/mmm	/mmm	/mmm	/mmm	/mmm
<b>a (Å)</b>	19.2242(3)	19.0525(3)	18.9132(4)	18.8897(2)	18.9190(3)
<b>b (Å)</b>	14.1563(2)	14.1166(2)	14.0833(3)	14.0629(1)	14.0492(1)
<b>c (Å)</b>	7.5106(1)	7.4953(1)	7.4843(2)	7.46808(6)	7.45785(7)
<b>V (Å<sup>3</sup>)</b>	2043.98(7)	2015.92(8)	1993.5(1)	1983.86(4)	1982.27(4)
<b>R<sub>p</sub> (%)</b>	5.84	5.36	5.79	6.03	5.78
<b>R<sub>wp</sub> (%)</b>	7.56	6.84	7.56	7.93	7.78
<b>R F**2 (%)</b>	9.68	9.81	11.38	13.03	16.75
<b>No. of variables</b>	85	90	90	89	90
<b>No. of observations</b>	9016	9016	9018	9018	9018
<b>No. of reflections</b>	1186	1171	1161	1153	1152

**Table 2** – Refined unit-cell parameters for ferrierite at various temperatures up to 670 °C.

T(°C)	a(Å)	b(Å)	c(Å)	v(Å <sup>3</sup> )
<b>30</b>	19.2242(3)	14.1563(2)	7.5106(1)	2043.98(7)
<b>50</b>	19.2122(3)	14.1563(2)	7.5106(1)	2042.28(7)
<b>100</b>	19.1721(3)	14.148(2)	7.5082(1)	2037.14(7)
<b>150</b>	19.1281(3)	14.1335(2)	7.5037(1)	2028.62(7)
<b>200</b>	19.0525(3)	14.1166(2)	7.4953(1)	2015.92(7)
<b>250</b>	18.9588(4)	14.0991(2)	7.4897(1)	2002.0(1)
<b>300</b>	18.9132(4)	14.0833(3)	7.4843(2)	1993.5(1)
<b>350</b>	18.8951(4)	14.0726(3)	7.4775(2)	1988.3(1)
<b>400</b>	18.8899(4)	14.0661(3)	7.4719(2)	1985.3(1)
<b>450</b>	18.8897(2)	14.0629(1)	7.46808(6)	1983.86(4)
<b>500</b>	18.8923(4)	14.0617(3)	7.4654(2)	1983.25(4)
<b>550</b>	18.8974(3)	14.0590(2)	7.4631(1)	1983.0(1)
<b>600</b>	18.9049(4)	14.0591(2)	7.461(1)	1983.04(1)
<b>650</b>	18.9137(4)	14.0549(3)	7.4592(1)	1982.9(1)
<b>670</b>	18.9190(3)	14.0492(1)	7.45785(7)	1982.27(4)



**Table 3** – Dimensions along the *a* axis of 10MR, 8MR and 6MR at 30, 200, 300, 450 and 670 °C

	<b>30°C</b>	<b>200°C</b>	<b>300°C</b>	<b>450°C</b>	<b>670°C</b>
<i>Projection along c</i>					
<b>10MR</b> <b>O8-O8 (Å)</b>	6.88	6.82	6.72	6.73	6.67
<b>6MR</b> <b>O3-O3 (Å)</b>	3.74	3.74	3.65	3.66	3.67
<i>Projection along b</i>					
<b>8 MR</b> <b>O7-O7 (Å)</b>	4.35	4.26	4.25	4.26	4.39

**Figure 1**



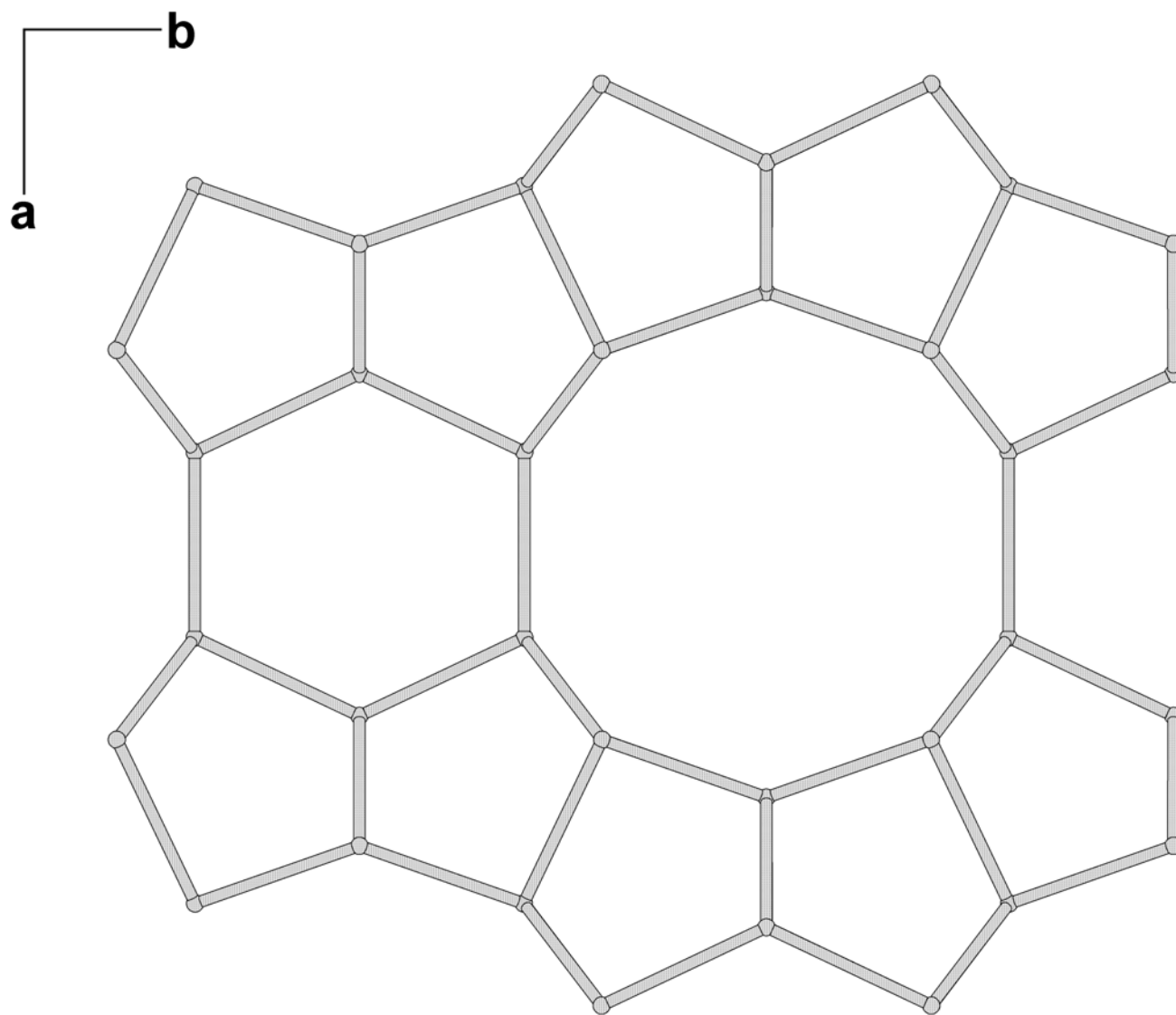


**Figure 2a**

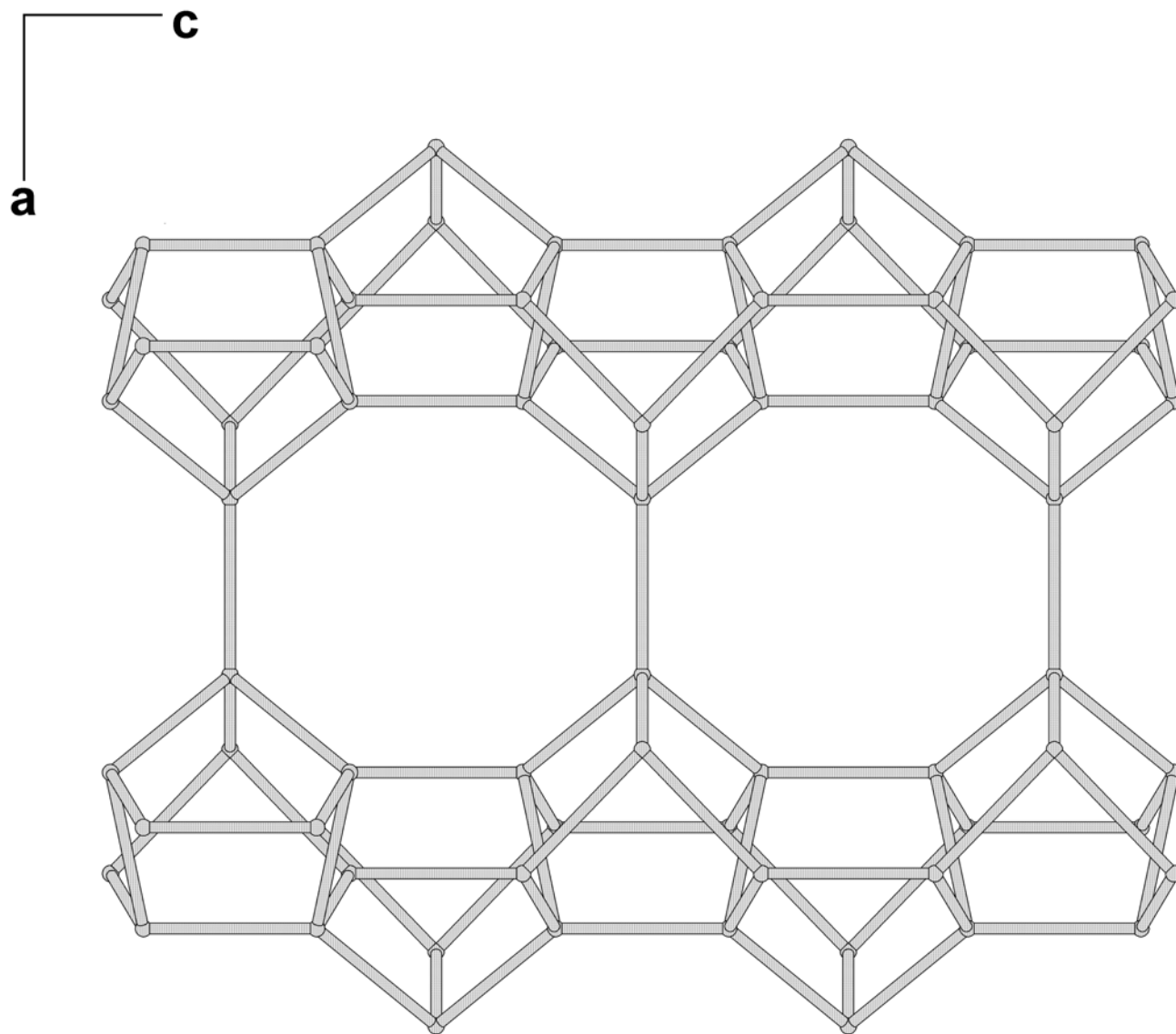


**Figure 2b**

Figure 3

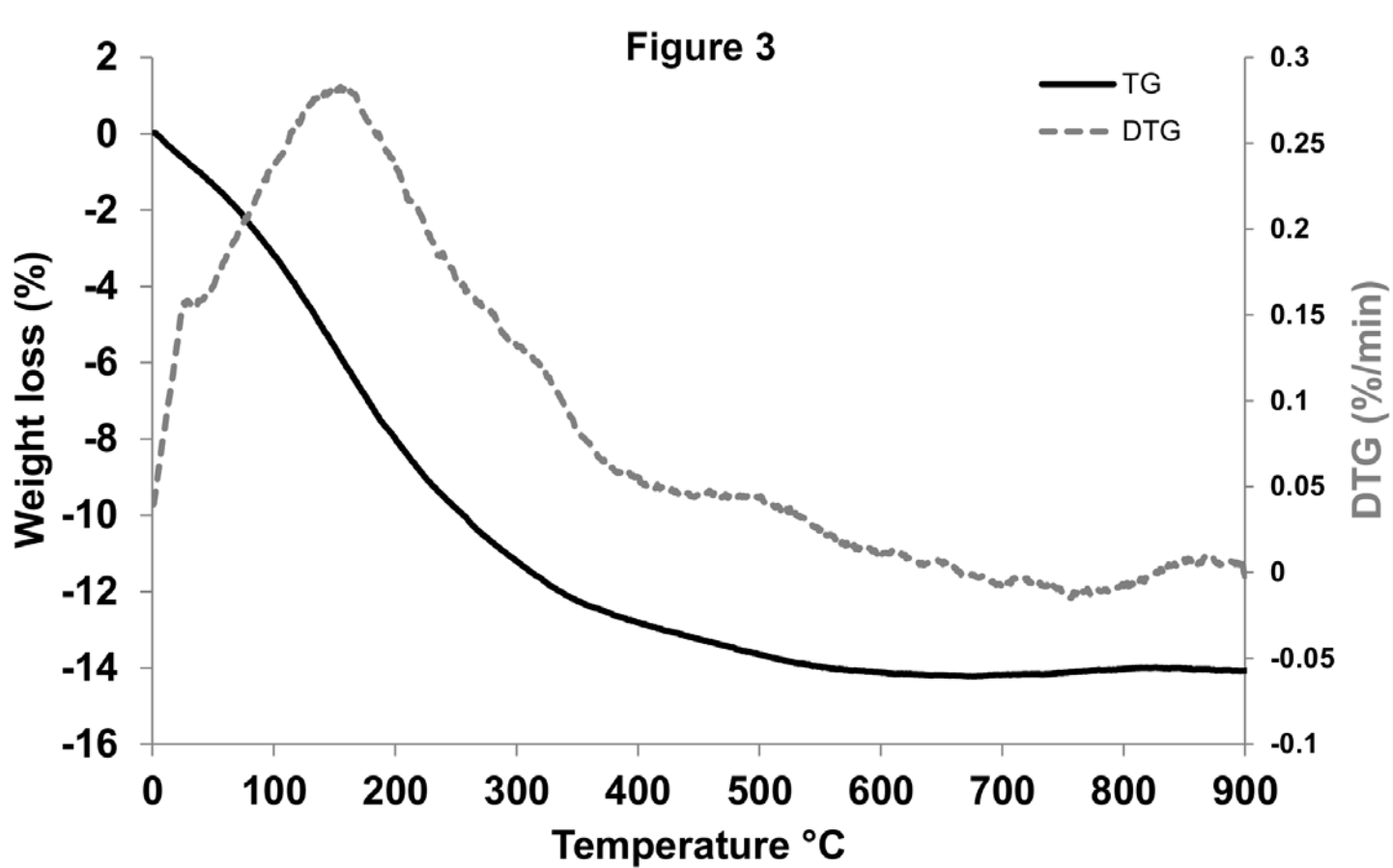


# Figure 5

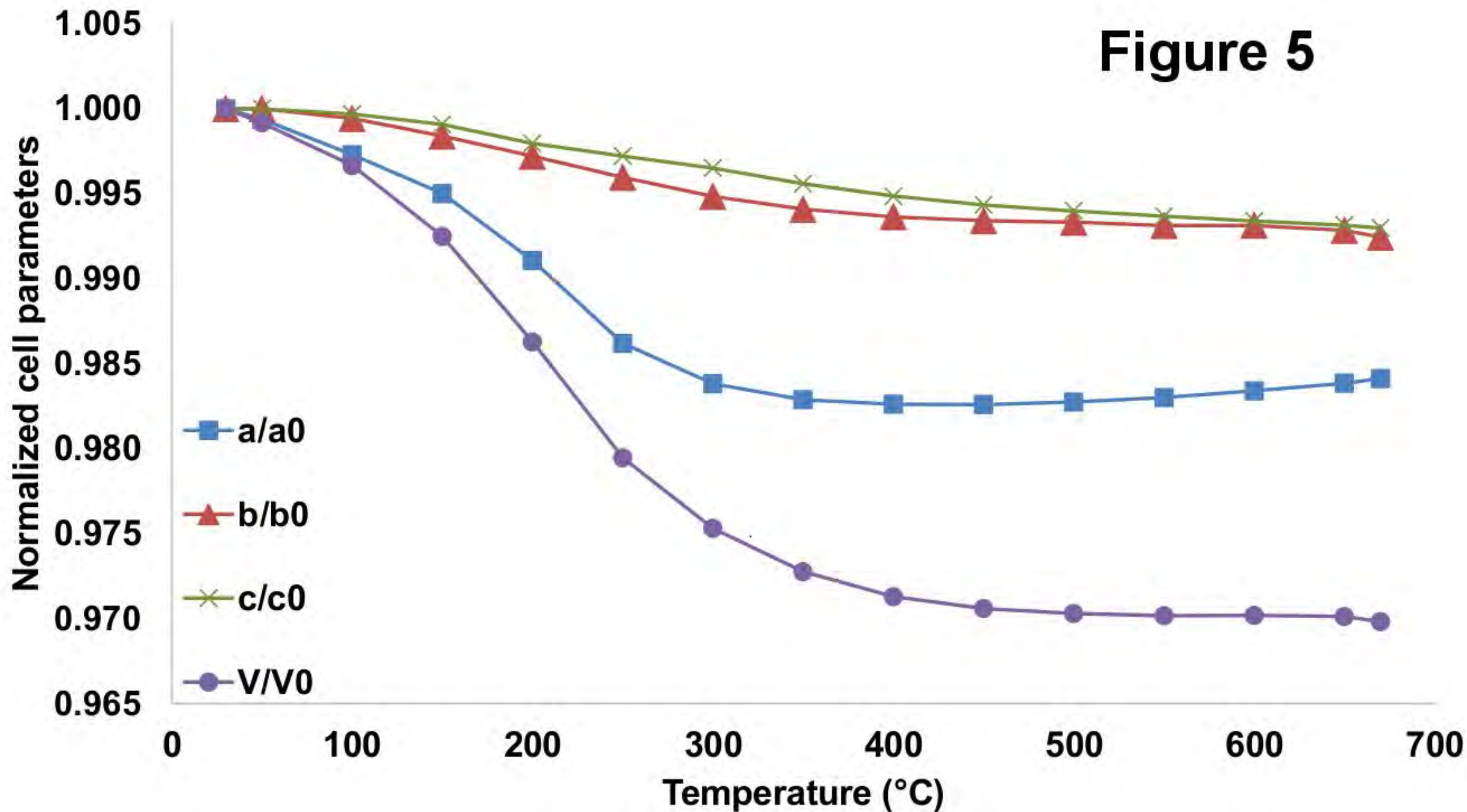
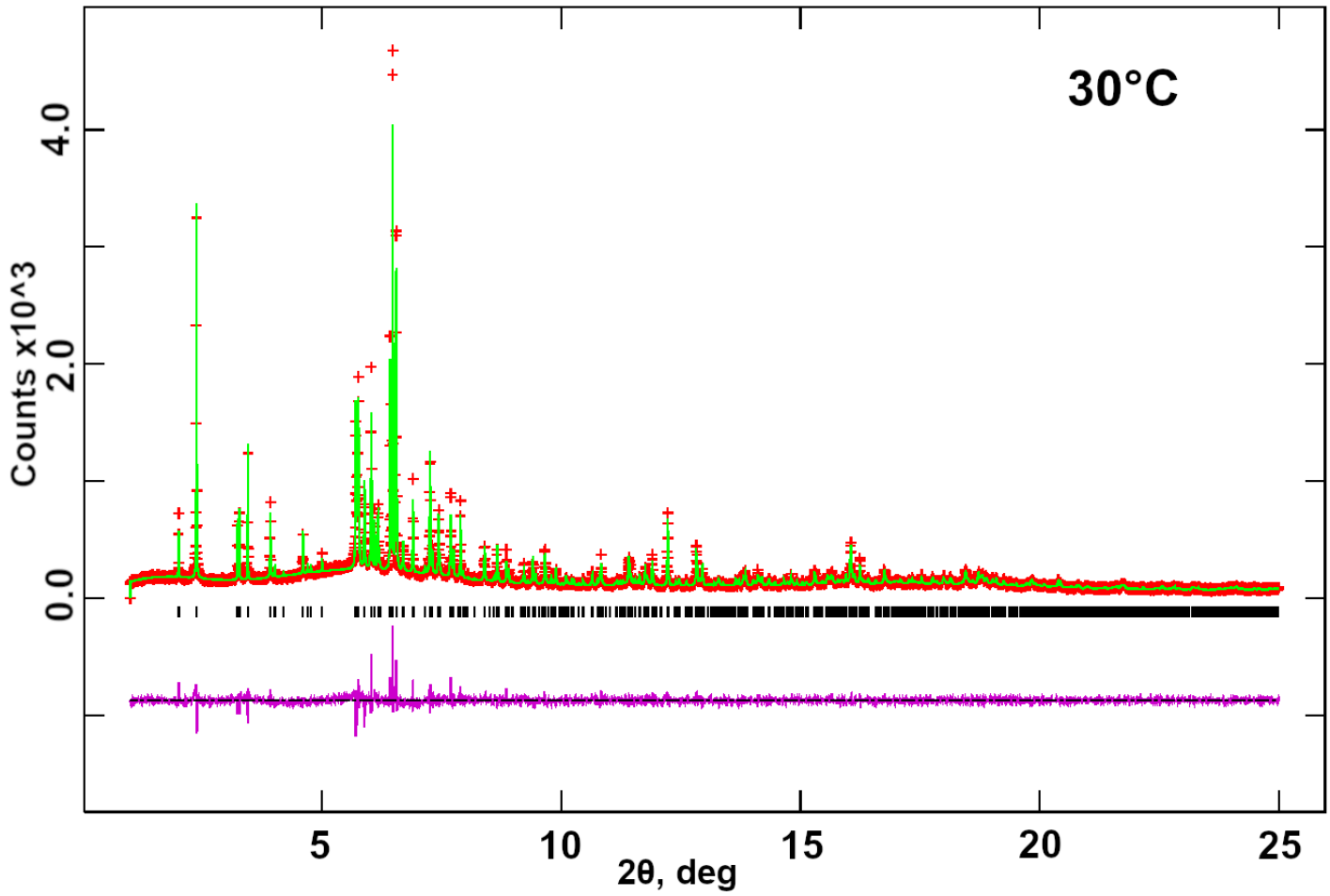
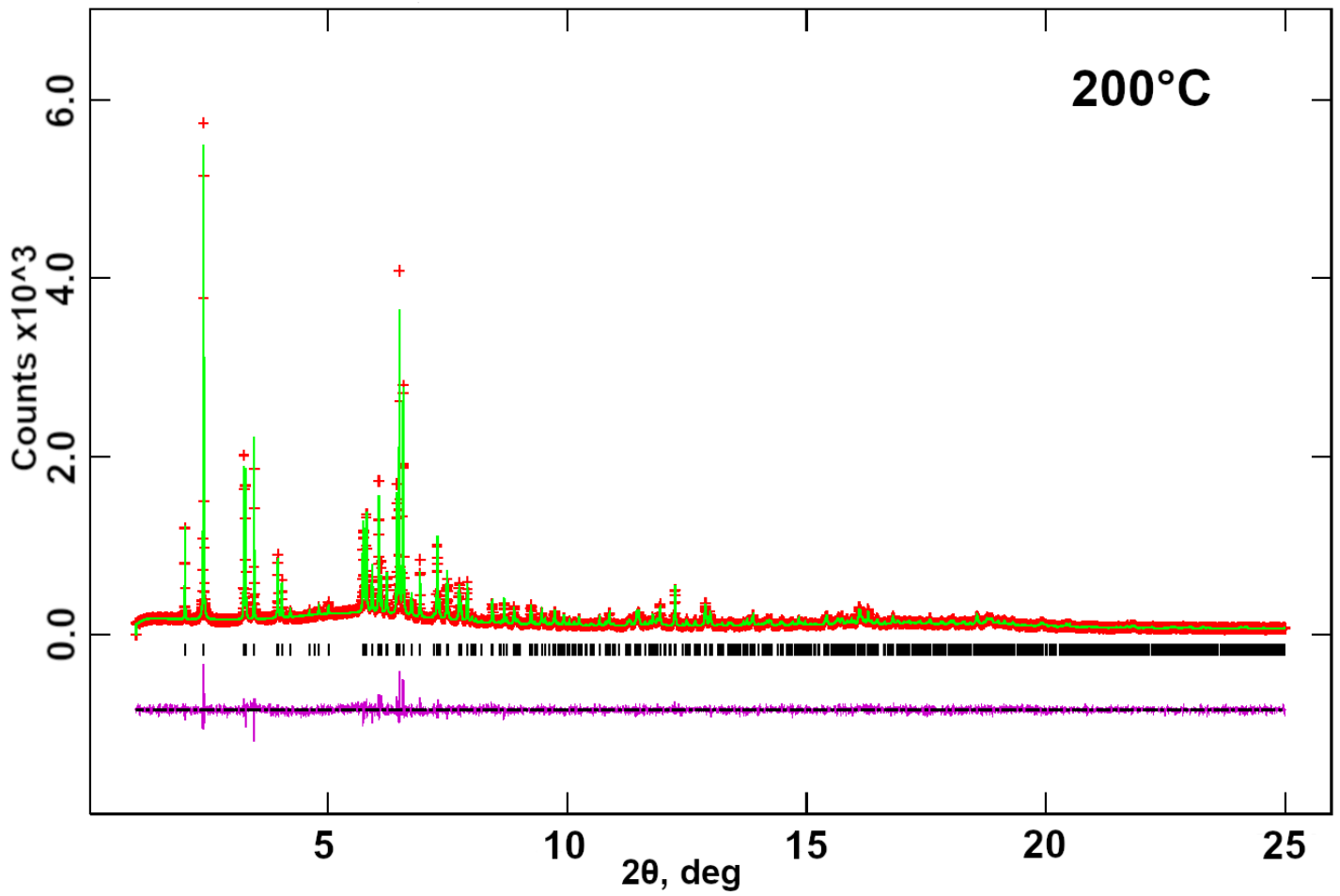


Figure 6Sa

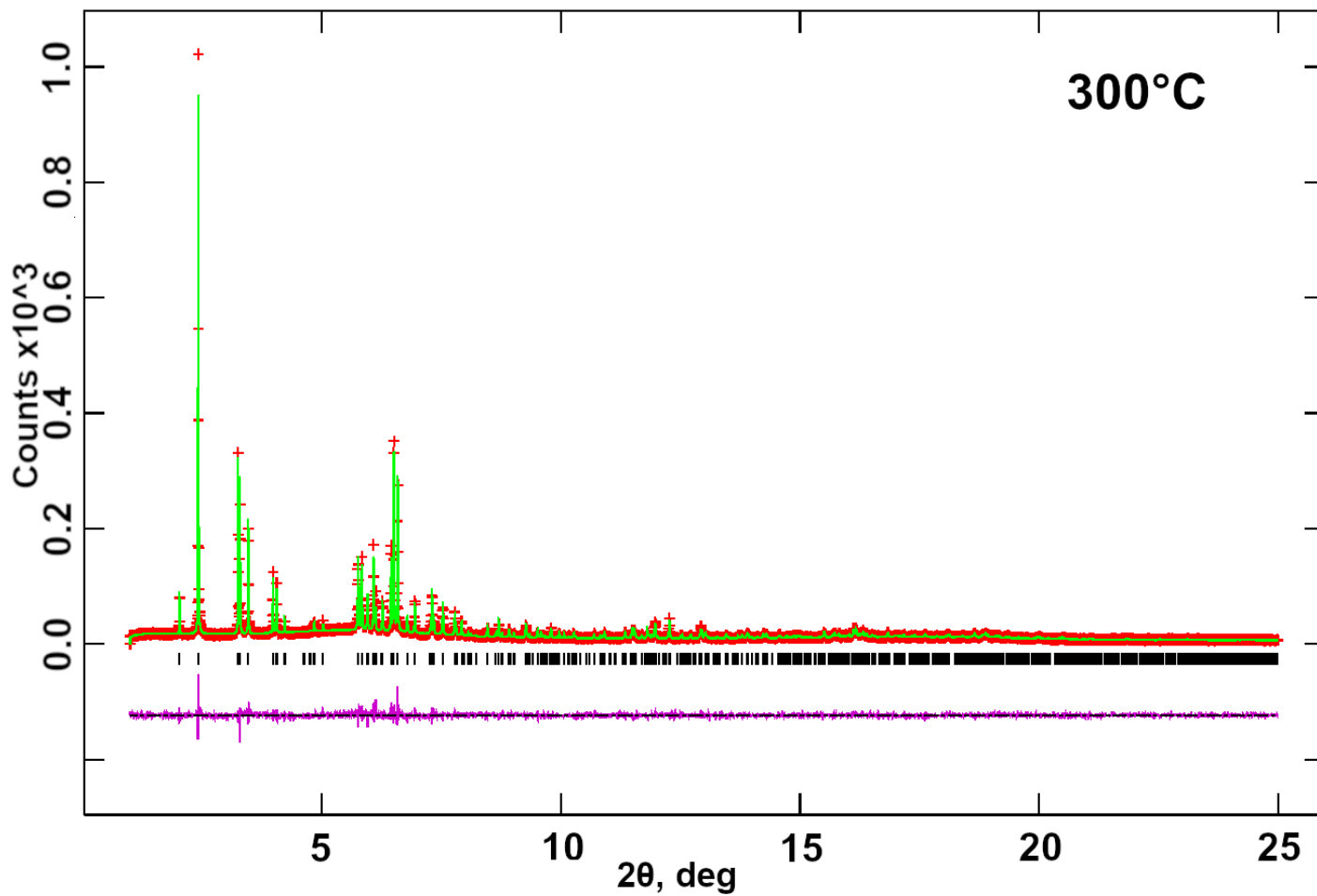


**Figure 6Sb**

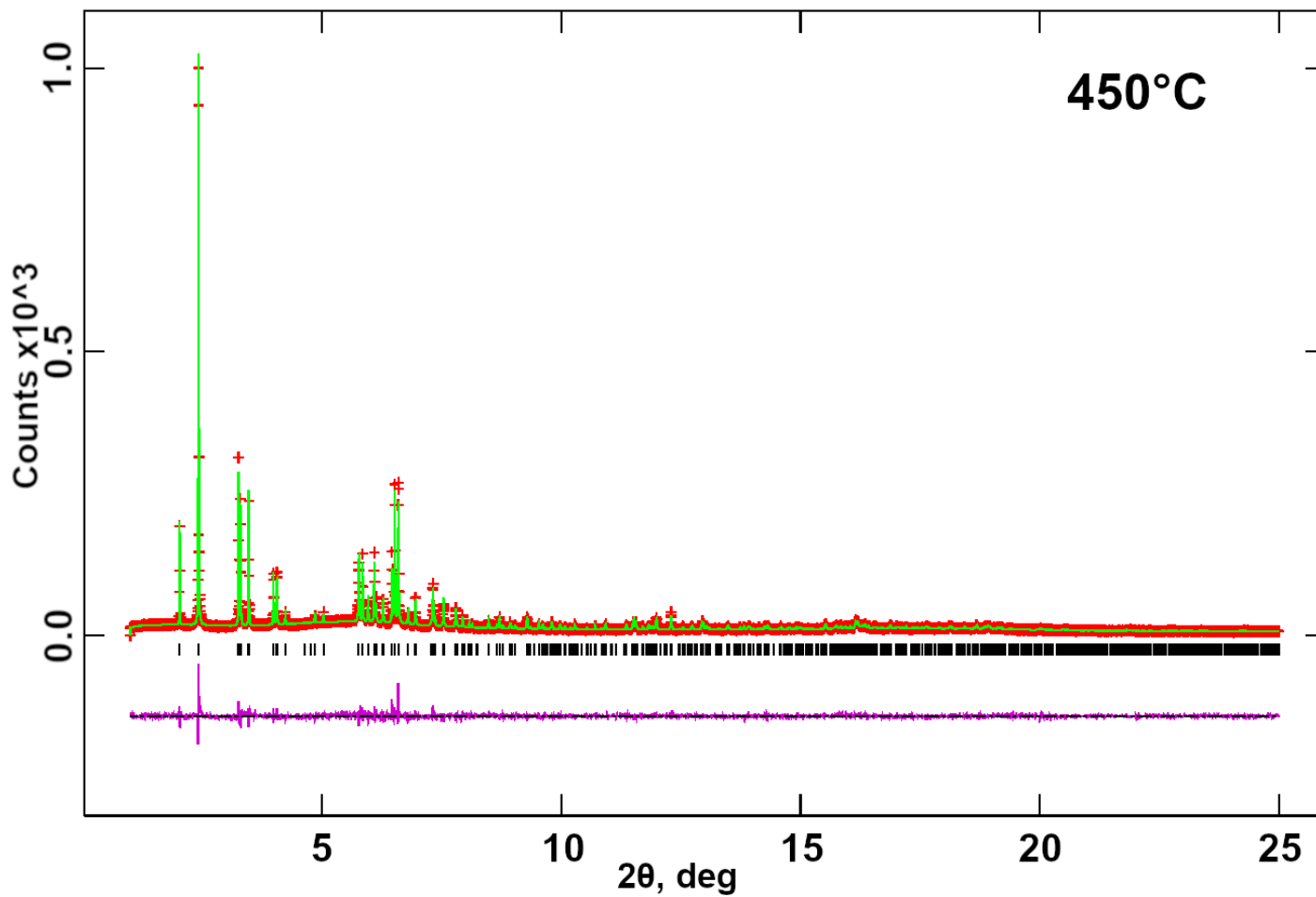




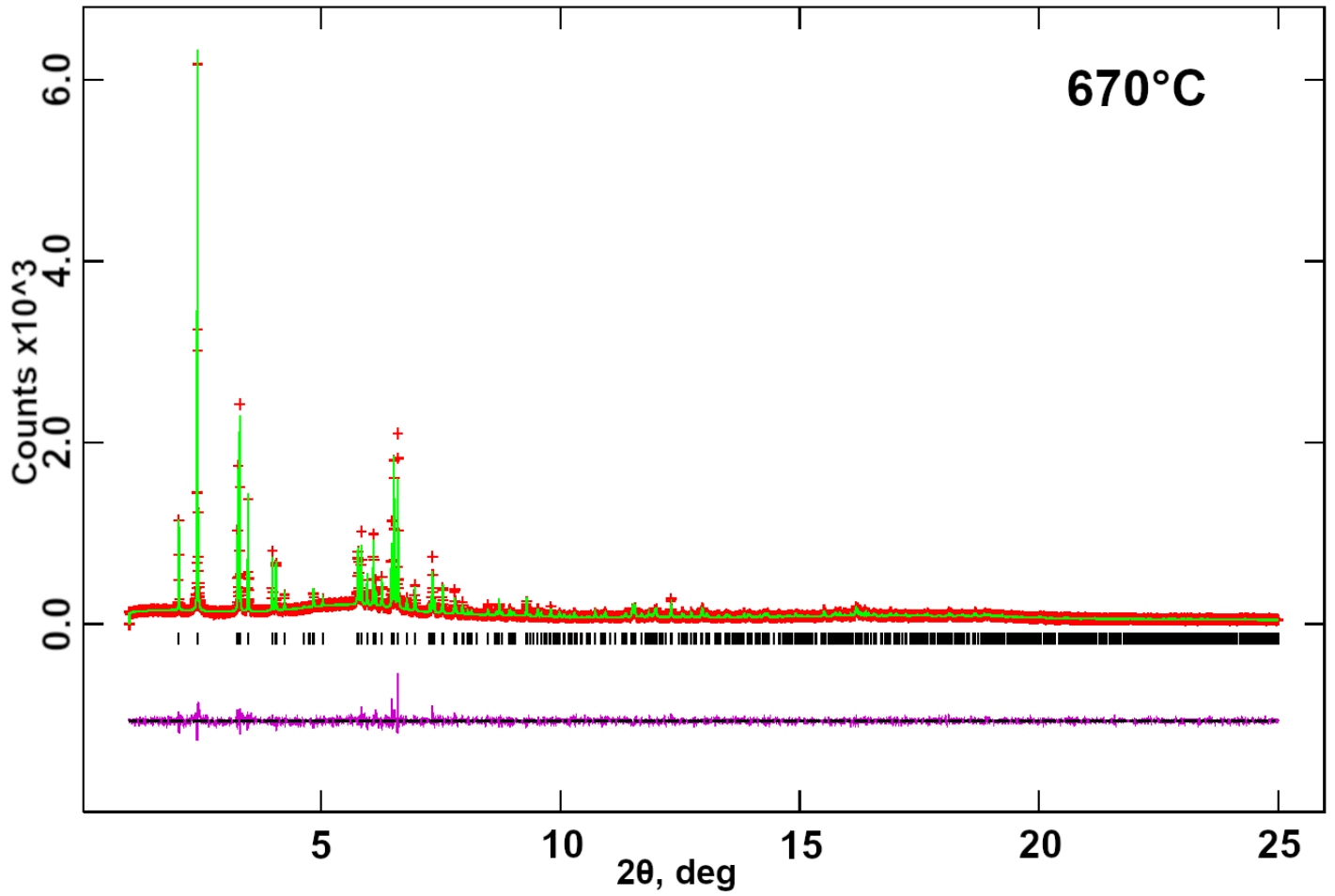
**Figure 6Sc**

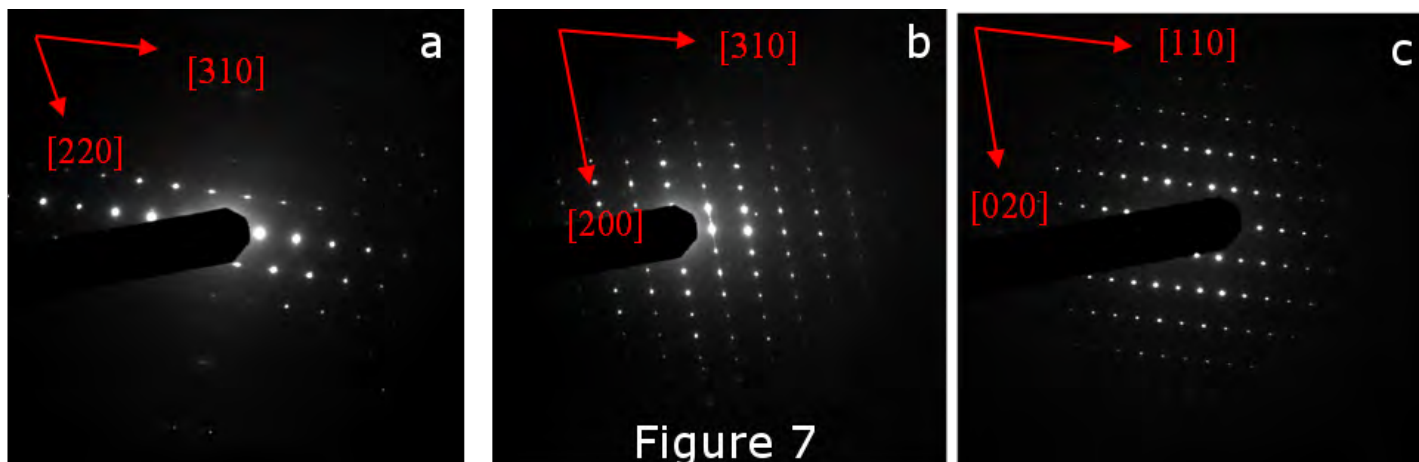


**Figure 6Sd**



**Figure 6Se**





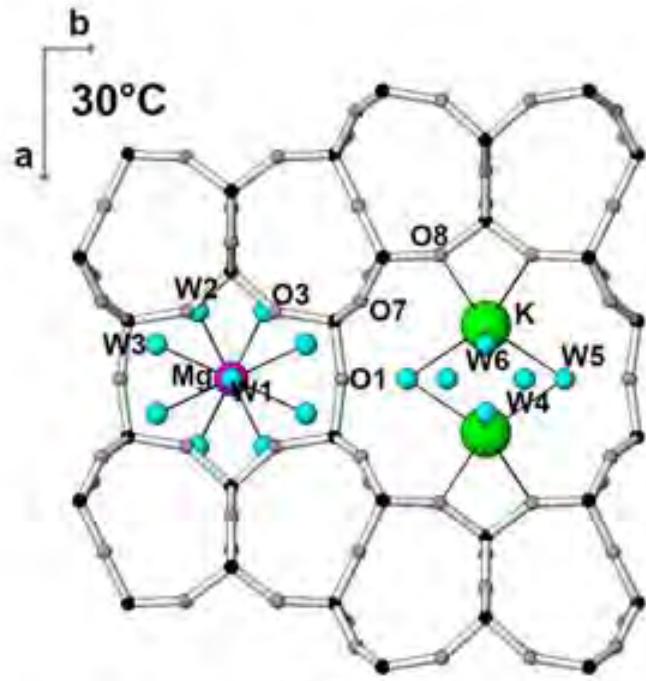


Figure 8a

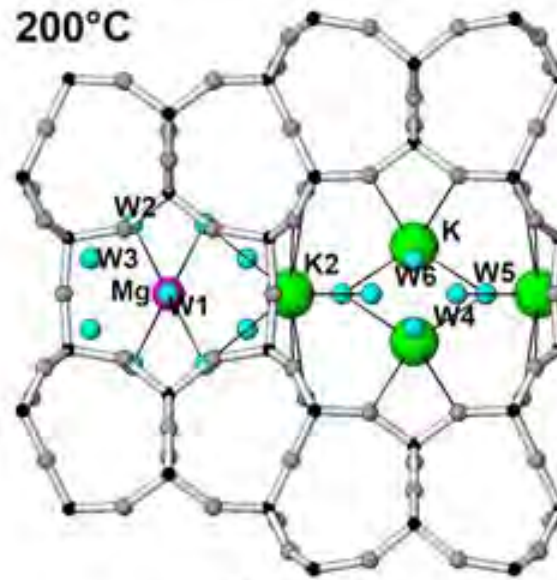


Figure 8b

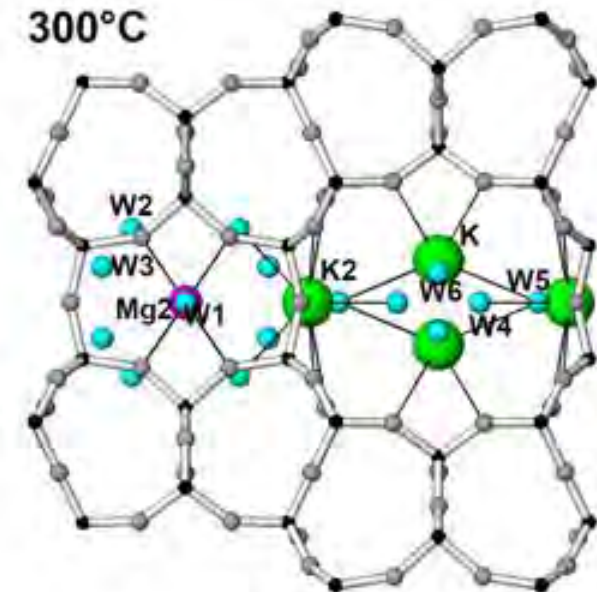


Figure 8c

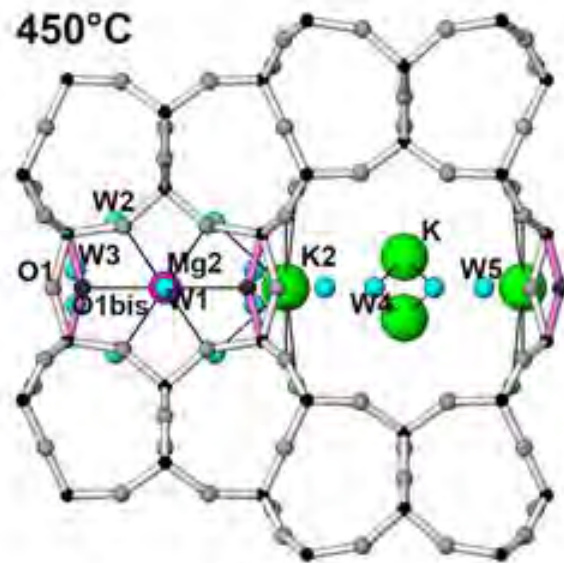


Figure 8d

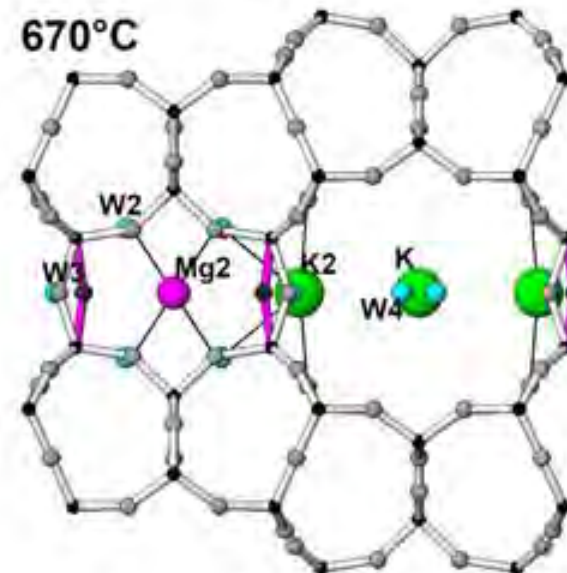


Figure 8e

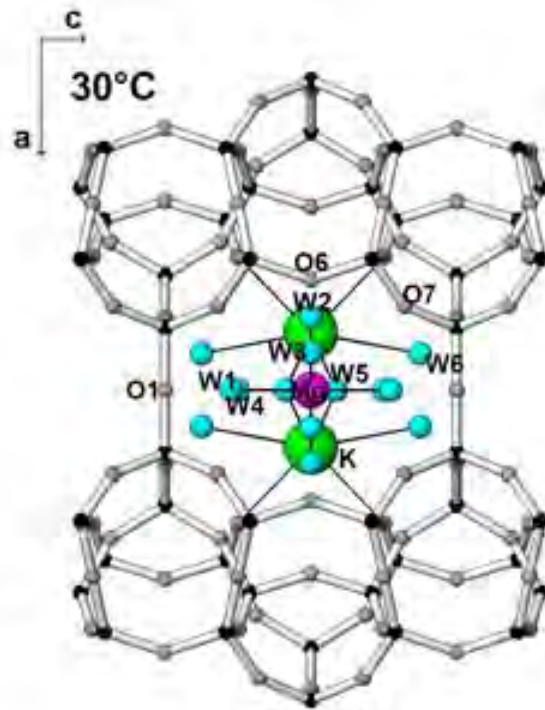


Figure 9a

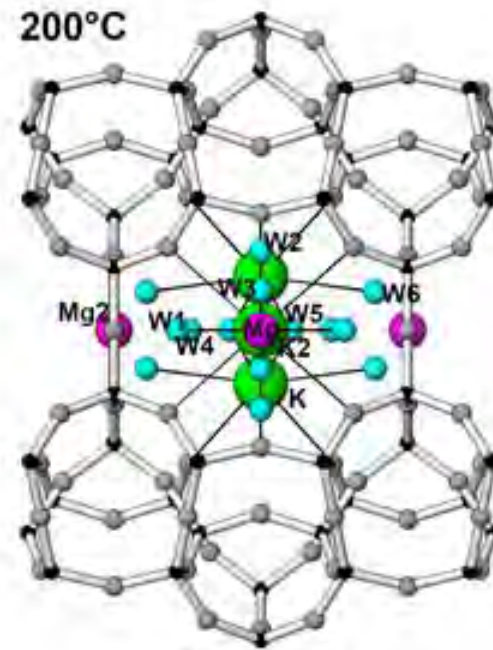


Figure 9b

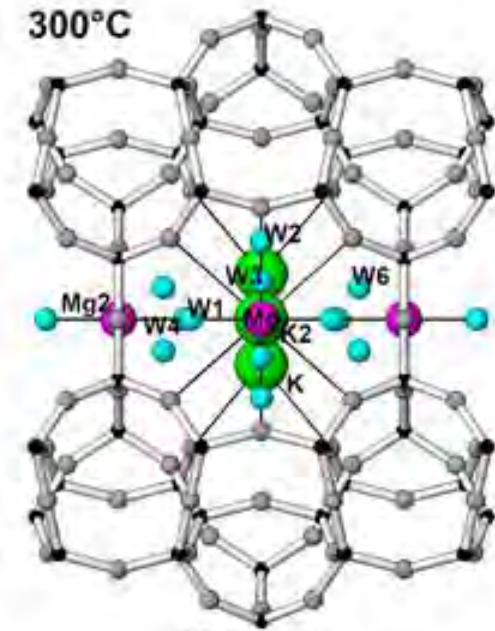


Figure 9c

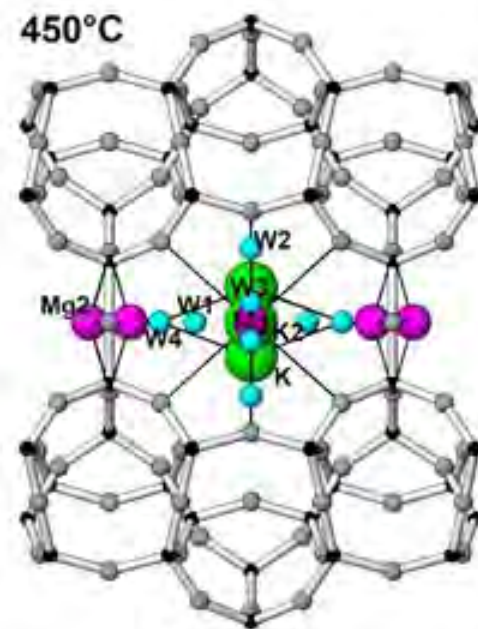


Figure 9d

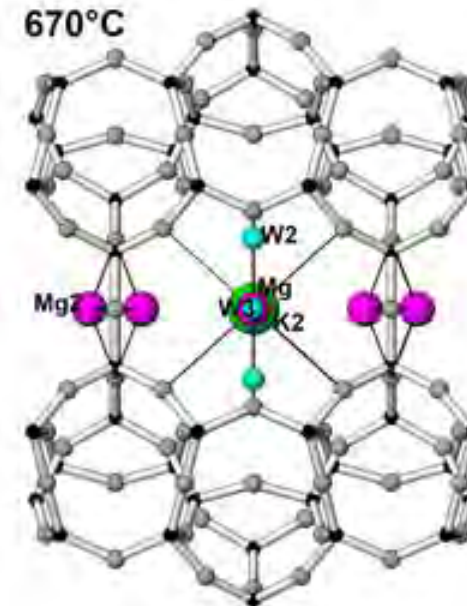


Figure 9e

